Small

NANO · MICRO small
www.small-journal.com

RESEARCH ARTICLE OPEN ACCESS

Invariant Photoinduced Energy-Transfer Followed by Electron-Transfer Events in Boron Dipyrromethene Derivatives Covalently Anchored to MoS_2 and WS_2

Ruben Canton-Vitoria[1] | Shuai Shao[2] | Habtom B. Gobeze[2] | Youngwoo Jang[2] | Francis D'Souza[2] | Nikos Tagmatarchis[1]

[1]Theoretical and Physical Chemistry Institute, National Hellenic Research Foundation, 48 Vassileos Constantinou Avenue, Athens, Greece | [2]Department of Chemistry, University of North Texas, Denton, Texas, USA

Correspondence: Francis D'Souza (Francis.DSouza@unt.edu) | Nikos Tagmatarchis (tagmatar@eie.gr)

Received: 13 November 2025 | **Accepted:** 8 December 2025

Keywords: boron dipyrromethene | charge-separation | covalent functionalization | electron-transfer | transition metal dichalcogenides

ABSTRACT

We report the covalent functionalization of exfoliated MoS_2 and WS_2 via a 1,2-dithiolane-based reaction using boron dipyrromethene (BODIPY) derivatives **1a-c** featuring either methyl, phenothiazine (PTZ), or triphenylamine (TPA) units at the α-carbons of BODIPY, shifting the light-harvesting capability of the MoS_2-based **2a-c** and WS_2-based **3a-c** hybrids from the visible to the near-infrared region. All new hybrids are comprehensively characterized via spectroscopic, thermal, and microscopy imaging techniques. Markedly, femtosecond transient absorption spectroscopy assays revealed a multi-step sequence of events under light illumination, beginning with energy transfer from the BODIPY derivatives to the TMDs, followed by electron-transfer from the excited TMDs to BODIPYs, forming a thermodynamically stable charge-separated state $TMD^{\bullet+}$-$BODIPY^{\bullet-}$. Interestingly, while the presence of electron-donating substituents of PTZ and TPA in BODIPY derivatives **1b-c** partially inhibits these processes, all hybrids **2a-c** and **3a-c** exhibit similar photoinduced electronic behavior, signifying that the electronic interface of MoS_2 or WS_2 and BODIPYs remains largely unaffected by the specific region of the electromagnetic spectrum from which light is harvested, the nature of TMDs, or their electron-donating/accepting character. While the rates of energy transfer, k_{ENT}, from ^{1}BODIPY* to TMD are within the time-resolution of our instrumental setup, the rate of electron transfer, k_{ET}, from ^{1}TMD* to BODIPY resulting in $TMD^{\bullet+}$-$BODIPY^{\bullet-}$ is in the range of $1–2 \times 10^9$ s^{-1}, revealing efficient charge separation in these hybrids.

1 | Introduction

Transition metal dichalcogenides (TMDs) are highly fascinating 2D semiconducting nanomaterials. Briefly, TMDs, featuring a three-atom-thick and large planar dimension network, possess excitonic absorption bands in the visible and near-IR region of the electromagnetic spectrum, and, in single-layered form, display significant emissive fluorescence in the range 550–1250 nm [1]. Notably, when TMDs are employed as field-effect transistors, the current can increase more than eight orders of magnitude, and thanks to the direct bandgap and ultralow binding energies of excitons (5–40 meV) [2], the incident light can tailor the conductivity of the material. In addition, TMDs demonstrate excellent flexibility and relatively strong chemical and mechanical resistance, thus overall, making them extremely appealing as essential components for energy conversion nanodevices [3–5].

Ruben Canton-Vitoria and Shuai Shao contributed equally to this work.

The chemical functionalization of TMDs with organic compounds is a widely employed approach to enhance their capabilities [6–8]. Particularly, covalent functionalization is a strategy with which the addends remain topologically locked at a specific distance and position over TMDs, while providing greater stability and reusability in wet media [2, 7]. Interestingly, interfacing chromophores with TMDs allows tailoring the optical and electronic characteristics of the hybrid material, increasing their use in energy conversion applications [9, 10]. The covalent functionalization of TMD nanosheets with large dimensions proved beneficial for device fabrication, whereas smaller nanosheets were more suitable for maximizing the level of functionalization, while preserving the intrinsic properties of the TMDs. In this respect, covalent incorporation of porphyrin [11] resulted, upon illumination, in energy transfer to MoS_2, while phthalocyanine [12] or pyrene [13] in electron donation to MoS_2. In addition, an electron-accepting perylene diimide derivative revealed the electronic alter-ego nature of MoS_2 [14]. Furthermore, the presence of covalently anchored carbon dots onto MoS_2 yielded the development of electron-transfer phenomena, whereas WS_2 merely absorbs energy [15]. However, all these processes involve a single action–reaction pathway, where light irradiation exclusively induces electron, hole, or energy transfer. Functionalization with a chromophore that enables multiple photoinduced events under a single incident light—for instance, an initial energy transfer that subsequently promotes electron transfer—remains elusive and warrants further investigation, offering an attractive strategy for nanotechnology and energy conversion applications.

Certainly, dyes can tune the semiconducting properties of TMDs through covalent functionalization, improving key parameters and increasing light conversion capabilities, which is of demonstrated interest in photocatalytic, biology, and nanotechnology applications [16–24]. Unfortunately, there is no straightforward strategy to predict the behavior of TMD–dye hybrids, as each dye exhibits a unique combination of electron-donating/accepting character, chromophoric structure, and specific light-harvesting range. In this context, it remains elusive how substituents on a single chromophoric center, capable of modulating the light-absorption region, affect the photophysical behavior of TMDs. To address this challenge, boron dipyrromethene (BODIPY) [25], with demonstrated strong electronic interactions with TMDs [26–28], has emerged. Moreover, BODIPY features a versatile chemistry that enables selective light harvesting from the blue to the NIR region, through derivatization with various photoactive species [29, 30]. For instance, when BODIPY is coupled with ferrocene, triphenylamine (TPA), or C_{60}, a multistep electron-transfer cascade can be triggered [31]. Moreover, BODIPY linked to zinc-porphyrin (ZnP) and C_{60} exhibits photoinduced energy-transfer processes, occurring first from BODIPY to ZnP, followed by electron transfer to C_{60} [32–34]. In contrast, graphene transfers electrons to ZnP or BODIPY [35, 36]. Hence, BODIPY is recognized for its optical tunability and broad range of excitonic transfer behaviors.

Notably, phenothiazine (PTZ) and triphenylamine (TPA) serve as electron-donating substituents, yet display minimal intrinsic light absorption. Although their donating strength is insufficient to alter the electron–hole-transfer character of BODIPY fundamentally, they reduce the HOMO–LUMO gap, thereby redshifting the system's light absorption from Vis-to-NIR. Indeed, BODIPY, BODIPY–PTZ, and BODIPY–TPA have been shown to undergo electron-transfer to C_{60}, achieving charge-separated states with energies of 2.43, 1.75, and 1.73 eV, respectively [37, 38]. These processes are particularly relevant to our investigation, which aims to understand how a single chromophoric core, substitutionally derivatized to harvest light from distinct regions of the electromagnetic spectrum, electronically interacts with TMDs. This field of research is unexplored and may result in interesting photoinduced charge-transfer phenomena.

Herein, BODIPY derivatives carrying a 1,2-dithiolane unit and either a methyl, PTZ, or TPA group were covalently anchored at sulfur vacancies of chemically exfoliated MoS_2 and WS_2, resulting in hybrid materials MoS_2-BODIPY **2a-c** and WS_2-BODIPY **3a-c**. All these newly prepared hybrids were spectroscopically and thermally characterized, and morphologically imaged by transmission electron and atomic force microscopy. More importantly, femtosecond transient absorption spectroscopy revealed ultrafast excited-state energy-transfer followed by electron-transfer in these novel donor–acceptor hybrids, proving stepwise electronic communication between TMDs and the various BODIPY chromophores.

2 | Results and Discussion

The synthesis of BODIPY derivatives **1a-c**, carrying a methyl, PTZ, or TPA group at the α-carbons of BODIPY, respectively, is shown in Scheme S1, along with the experimental details and relevant characterization data (Figures S1–S6). The presence of 1,2-dithiolane ring in BODIPYs **1a-c** allows the covalent anchorage onto exfoliated MoS_2 and WS_2 [9, 21], yielding MoS_2-based **2a-c**, and WS_2-based **3a-c** hybrids, respectively (Figure 1).

Attenuated-total-reflectance infrared (ATR-IR) spectroscopy provided evidence that BODIPY derivatives are successfully integrated onto exfoliated TMDs. In particular, compound **1a** and hybrids **2a** and **3a** exhibit strong alkyl C—H stretching and bending modes, within the range 2850–2970 cm^{-1}, while the carbonyl ester and the C═C vibrations are found at 1750 and 1464 cm^{-1}, respectively (Figure 2a). Similarly, IR bands deriving from BODIPYs **1b-c** are evident in hybrids **2b-c** and **3b-c** (Figure S7a,b).

Raman spectroscopy of hybrids **2a** and **3a**, upon excitonic in-resonance excitation at 633 nm for MoS_2 and at 514 nm for WS_2, shows the A_{1g} (407 cm^{-1} in MoS_2, and 419 cm^{-1} in WS_2), E^1_{2g} (383 cm^{-1} in MoS_2, and 355 cm^{-1} in WS_2) and 2LA(M) (460 cm^{-1} in MoS_2, and 350 cm^{-1} in WS_2) modes [15–24], in addition to BODIPY signatures associated with the aromatic rings in the range 1250–1600 cm^{-1} (Figure 2b,c). Of particular significance is the intensity of 2LA(M) mode, as it provides crucial insights into defect density within MoS_2 and WS_2. Once sulfur atoms of the 1,2-dithiolane ring in **1a-c** covalently fill the chalcogen vacant sites at TMD edges, the defects diminish, and consequently, the intensity of 2LA(M) mode in all hybrids **2a-c** and **3a-c** (Figure 2b,c; Figure S7c–f) is reduced [15–24]. Raman spectral mapping of the intensity ratio 2LA(M)/A_{1g} for exfoliated MoS_2 and hybrids **2a-c** (inset Figure 2b; Figure S7c,d) and for WS_2 and hybrids

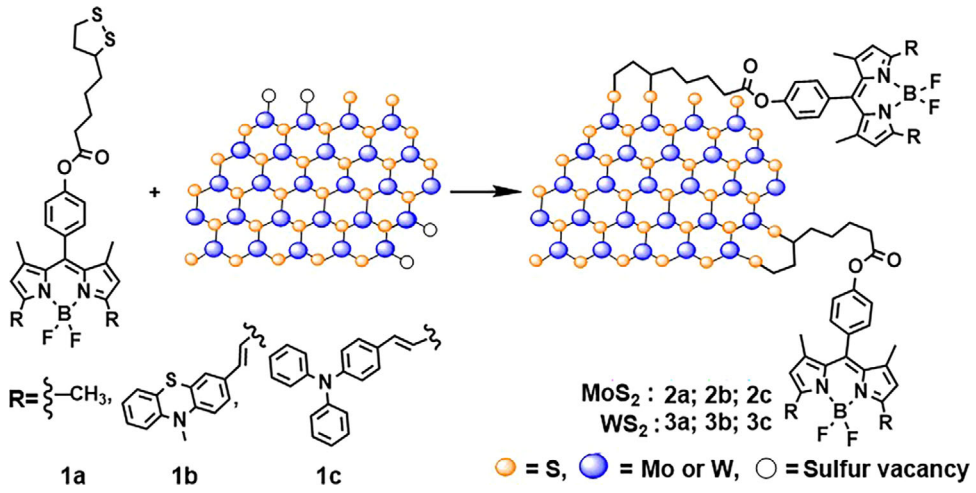

FIGURE 1 | Illustrative preparation of MoS_2-BODIPY **2a-c** and WS_2-BODIPY **3a-c** hybrid materials.

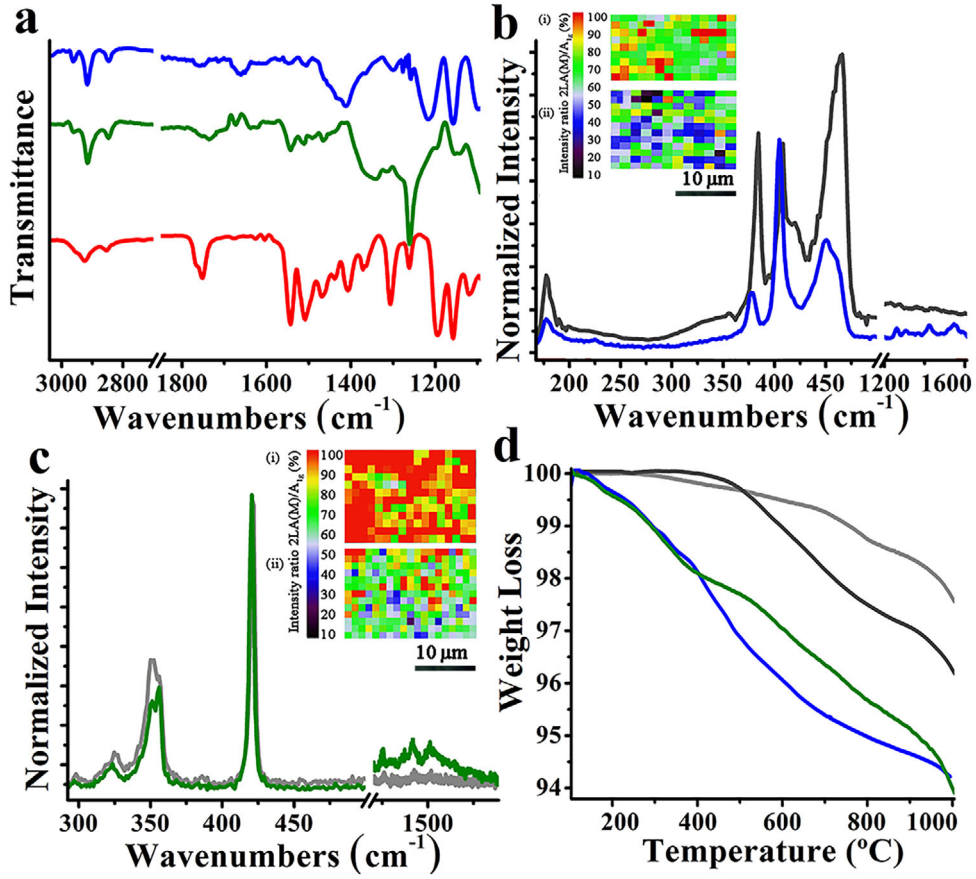

FIGURE 2 | (a) ATR-IR spectra for **1a** (red) and hybrids **2a** (blue) and **3a** (olive). (b) Raman spectra (633 nm) for exfoliated MoS_2 (dark gray) and hybrid **2a** (blue). Inset: Raman spectral map intensity ratio of $2LA(M)/A_{1g}$ for (i) exfoliated MoS_2 and (ii) hybrid **2a**. (c) Raman spectra (514 nm) for exfoliated WS_2 (soft gray) and hybrid **3a** (olive). Inset: Raman spectral map intensity ratio of $2LA(M)/A_{1g}$ for (i) exfoliated WS_2 and (ii) hybrid **3a**. (d) TGA graphs for exfoliated MoS_2 (dark gray), exfoliated WS_2 (soft gray), and hybrids **2a** (blue) and **3a** (olive), obtained under nitrogen atmosphere.

3a-c (inset Figure 2c; Figure S7e,f), ensures the homogeneity of the covalent functionalization reaction with **1a-c** in **2a-c** and **3a-c**.

Thermogravimetric analysis (TGA) allows for the calculation of the loading of BODIPYs onto modified TMDs. First, exfoliated MoS_2 and WS_2 exhibit an incremental weight loss of 2% within the temperature range of 600–1000°C, being entirely stable at lower temperatures. In contrast, hybrids **2a** and **3a** display a weight loss of 3% and 2.2%, respectively, at the lower temperature range of 200–600°C, corresponding to the presence of BODIPY **1a** (Figure 2d). Similar weight loss values are observed for the thermal degradation of hybrids **2b-c** and **3b-c** (Figure S7g,h, respectively). In fact, the BODIPY loading in hybrids **2a-c** and

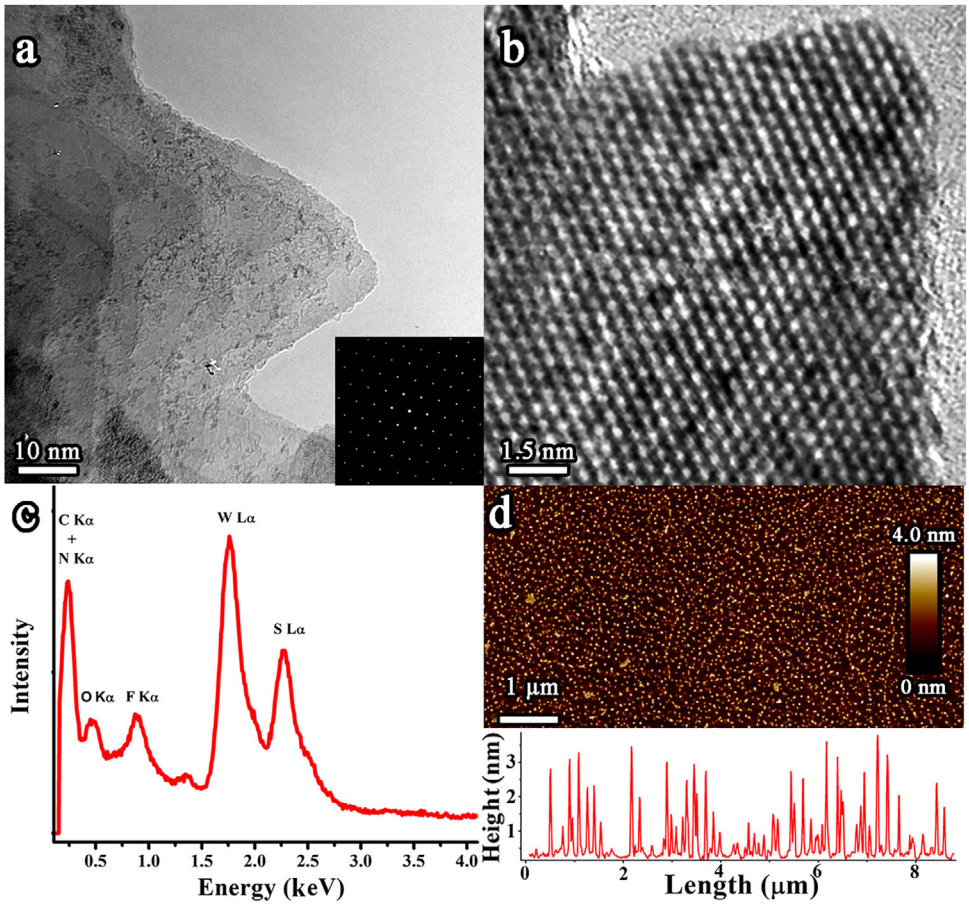

FIGURE 3 | (a,b) HR-TEM images and SAED pattern (inset), (c) EDS, and (d) AFM image and height profile of hybrid **3b**.

3a-c is about one group for every 35–65 MoS_2 and WS_2 units, respectively.

Morphological analysis of **2a-c** and **3a-c** was carried out using TEM and AFM. High-resolution bright-field TEM images reveal the layered structure characteristic of MoS_2 or WS_2. Specifically, hybrid **3b** (Figure 3a) shows no visible holes or cracks and displays smooth, well-defined edges. In addition, selected area electron diffraction (SAED) confirms a hexagonal lattice, indicating a predominant H-phase (Figure 3a, inset). At higher magnification (Figure 3b), the hexagonal arrangement of atoms in **3b** is clearly visible, confirming that the material's crystallinity is preserved after functionalization. Darker contrast near the edges may indicate the presence of BODIPY, further supported by EDS analysis, which detects target elements such as fluorine, with an F Kα at 0.68 keV [26, 35], beyond lighter elements such as nitrogen or carbon (Figure 3c). To minimize flake aggregation, a spin-coating technique was employed, yielding isolated ultrathin nanoflakes as observed by AFM [14]. These flakes exhibit lateral dimensions ranging from 50–150 nm and thicknesses between 1–5 nm (Figure 3d). Similar TEM-EDS and AFM morphologies were observed for hybrids **2a**-**c**, **3a**, and **3c** (Figure S8).

XPS analysis further confirmed the covalent bonding between TMD and BODIPY in **2a-c** and **3a-c**. Hybrids **2a** and **3a** were selected as representative examples (Figure 4), while data for the rest materials are provided in Figure S9. The presence of distinct Mo $3d_{5/2}$ and $3d_{3/2}$ peaks at 230.0 and 233.2 eV in **2a-c**, and of W $4f_{7/2}$, $4f_{5/2,}$ and $3f_{5/2}$ peaks at 33.0, 35.2, and 38.2 eV in **3a-c**, respectively, was confirmed. For **2a-c** and **3a-c**, the C 1s core level exhibits multiple components assigned to C═C (284.7 eV), C—C (285.3 eV), C—S (286.3 eV), C═N (287.0 eV), C—O (288.0 eV), and C═O (289.5 eV), the N 1s signal at 400.0 eV is consistent with the pyrrolidine group, and the B 1s peak at 186.5 eV confirms the presence of boron. The most compelling evidence for covalent bonding arises from analysis of the S 2p orbital. Both exfoliated MoS_2 and WS_2 display characteristic S $2p_{3/2}$ and S $2p_{1/2}$ doublets at 162.2 and 163.4 eV, attributed to the 2H phase. Additionally, satellite shoulders at 161.9 and 163.1 eV are observed, likely corresponding to sulfur vacancies or defect sites [9, 18, 19, 39]. Upon functionalization, the sulfur peaks undergo notable shifts of + 0.8 eV in **2a-c** and + 0.2 eV in **3a-c**. These shifts and peak transformations are attributed to electron-transfer between TMD layers and the BODIPY unit [20, 40]. Moreover, the S $2p_{3/2}$ and S $2p_{1/2}$ satellite features vanish, likely due to vacancy coverage by the 1,2-dithiolane functional group of BODIPYs. This provides direct evidence of covalent functionalization, resulting in a single doublet at 162.9 and 164.2 eV for **2a-c**, and 162.4 and 163.5 eV for **3a-c**, respectively.

The newly prepared hybrids exhibit the typical solubility of modified TMDs in certain organic solvents. In particular, **2a-c** and **3a-c** form stable dispersions at a concentration of 1 mg/mL in toluene, benzonitrile, and DMSO. This solubility opens the way to perform spectroscopic studies in liquid media, especially for understanding their behavior under illumination within the

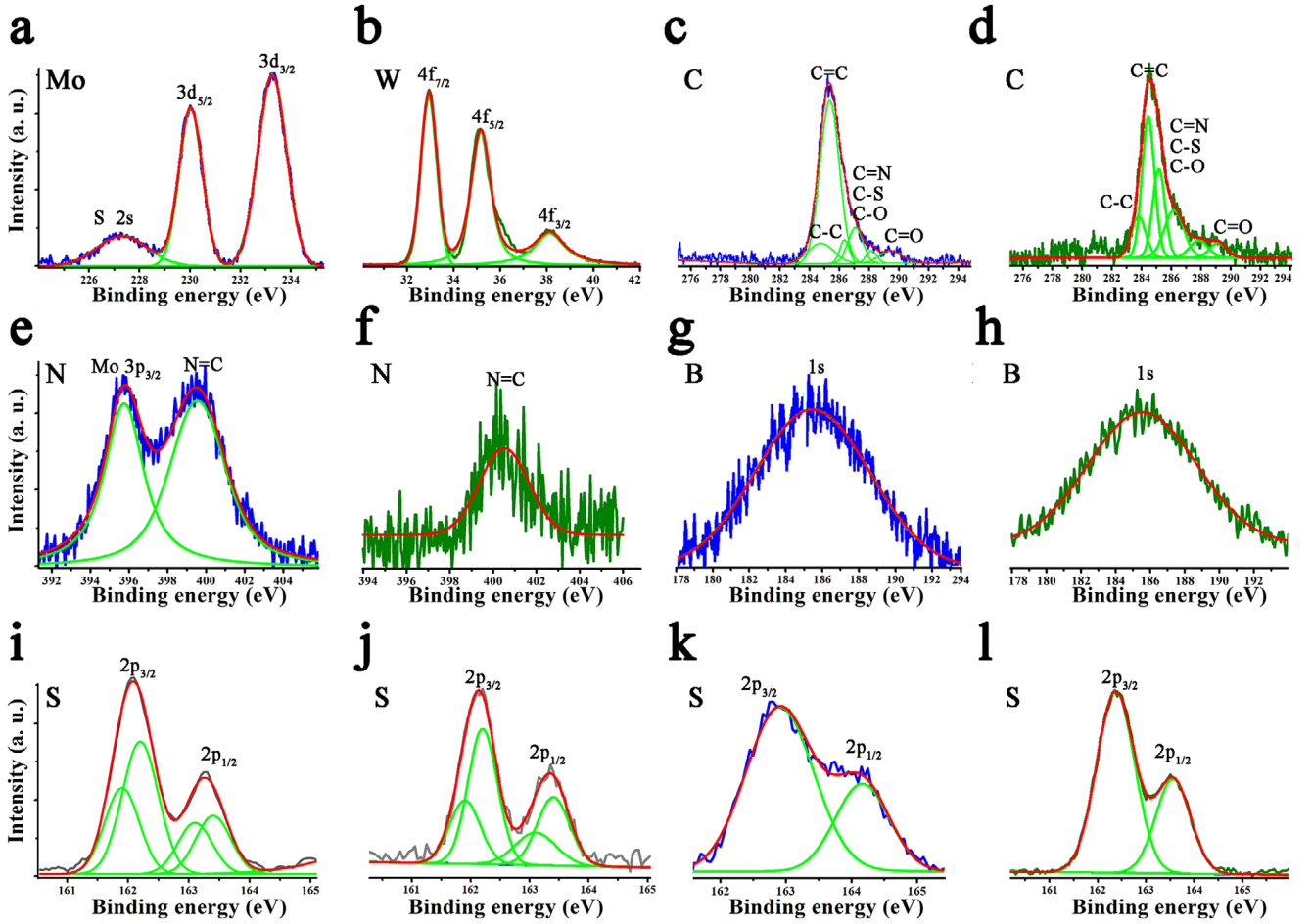

FIGURE 4 | XP spectra of (a,c,e,g,k) Mo 3d, C 1s, N 1s, B 1s, and S 2p orbitals for **2a**, (b,d,f,h,l) W 4f, C 1s, N 1s, B 1s, and S 2p orbitals for **3a**, (i) S 2p for exfoliated MoS_2, and (j) S 2p for exfoliated WS_2, respectively.

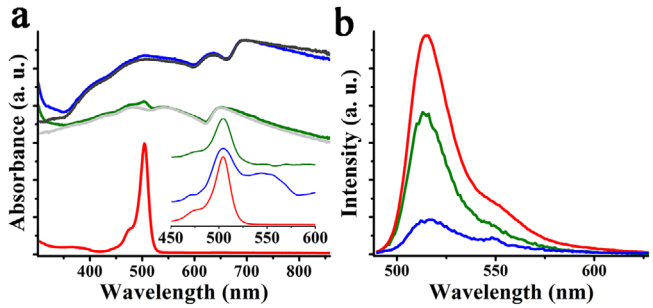

FIGURE 5 | (a) UV–vis absorption spectra for **1a** (red), exfoliated MoS_2 (dark gray), exfoliated WS_2 (light gray), and hybrids **2a** (blue) and **3a** (olive). Inset: UV–vis spectra in which the absorption due to MoS_2 and WS_2 is subtracted. (b) Photoluminescence spectra (excitation 470 nm) for **1a** (red) and hybrids **2a** (blue) and **3a** (olive). All spectra were obtained in toluene.

context of charge-transfer processes. The electronic absorption spectrum of BODIPY **1a** shows a distinctive band at 500 nm (Figure 5a). Derivatization of BODIPY with PTZ and TPA units, in **1b** and **1c**, shifts the maximum absorption to 685 nm (Figure S10a) and 694 nm (Figure S10b), respectively, demonstrating significant orbital mixing and electronic interactions between the substituted species. On the other hand, hybrids **2a-c** display the typical excitonic bands due to the semiconducting character of MoS_2 at 400, 500, 630, and 690 nm, and **3a-c** of WS_2 at 410,481, 545, and 652 nm, in addition to the bands derived from BODIPY (Figure 5a; Figure S10a,b). Appreciable ground-state electronic interactions of BODIPY–PTZ, and BODIPY–TPA with MoS_2 and WS_2, within **2b**-**c** and **3b**-**c**, occur, evident by the redshift of the BODIPY absorption band by 11, 9, and 12 nm in **2b**, **2c,** and **3b**, respectively, and by a 6 nm blueshift in **3c**. In contrast, hybrids **2a** and **3a** show simple superposition of absorption bands of BODIPY with TMDs, showcasing the absence of appreciable ground-state electronic interactions.

Examining the photophysical properties, a strong electronic communication between TMDs and the BODIPY derivatives **1a-c**, within hybrids **2a-c** and **3a-c**, was observed. First, based on steady-state photoluminescence assays, the distinctive emission band of BODIPY in **1a**, positioned at 514 nm (Figure 5b), is redshifted to 720 nm upon incorporation of the PTZ and TPA units, in **1b-c**, as shown in Figure S10c,d, respectively. This observation is in line with the aforementioned UV–vis studies. Furthermore, the emission of BODIPY derivatives **1a-c** was largely quenched by the presence of MoS_2 and WS_2 within hybrids **2a-c** and **3a-c**, for materials possessing equal absorption at the excitation wavelength (470 nm for **1–3a**, and 680 nm for **1b-c**, **2b-c**, and **3b-c**). In addition, the emission of BODIPY in **1c** was blueshifted, by the presence of WS_2 in **3c**, to 718 nm. These findings suggest intra-hybrid transduction of electron or energy

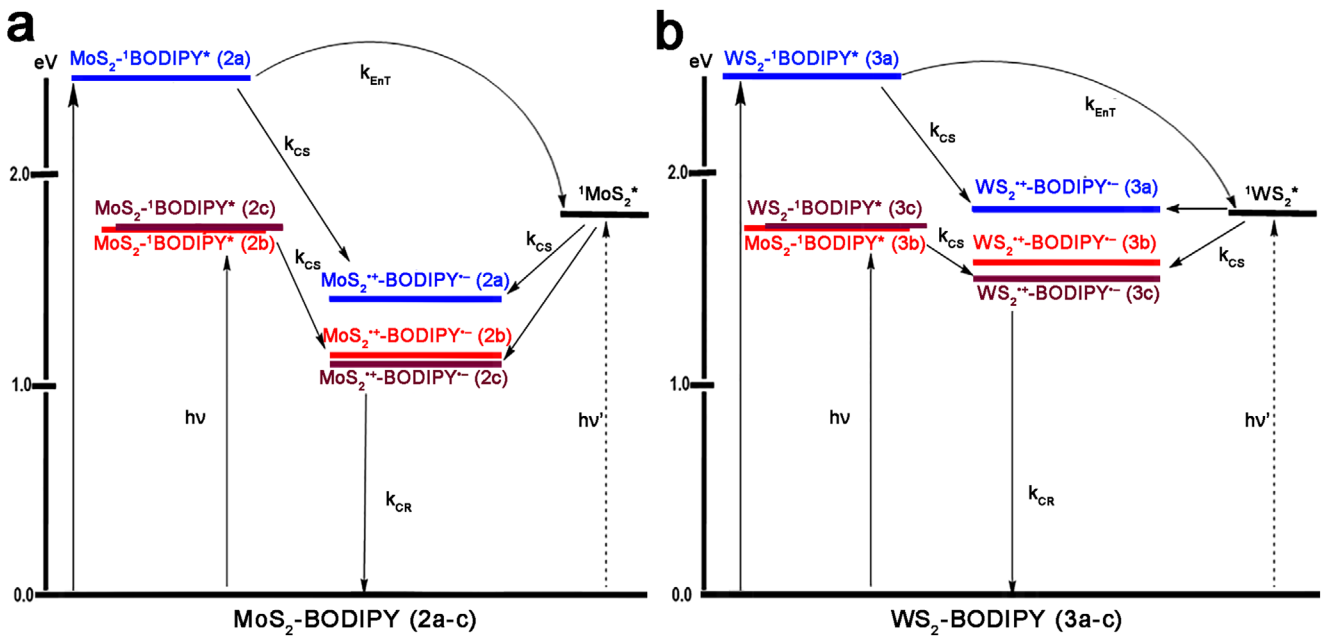

FIGURE 6 | Energy level diagrams showing different photochemical processes in (a) MoS_2-BODIPY hybrids **2a-c**, and (b) WS_2-BODIPY hybrids **3a-c**. Wherein hν and hν' correspond to the primary and secondary photoexcitation, respectively, k_{CS} and k_{EnT} are the rate constants of charge separation and energy transfer, and k_{CR} represents the recombination rate constant. Note that non-involved states have been omitted to simplify the diagram.

from the singlet excited-state of ^{1}BODIPY* to MoS_2 and WS_2 for hybrids **2a-c** and **3a-c**.

Having both photo- and redox-active entities within hybrid materials **2a-c** and **3a-c**, the energy level diagram based on free-energy change for charge separation states was constructed (Figure 6) to visualize the potential photochemical processes [15, 37, 38]. From such energy diagrams, it is clear that excited-state energy-transfer from singlet excited-state of ^{1}BODIPYs* **1a-c** to both MoS_2 and WS_2 in hybrids **2a-c** and **3a-c**, respectively, is thermodynamically feasible. It is important to note that MoS_2 and WS_2 exhibit strong absorption across the entire visible range (350–860 nm), which encompasses both the absorption and emission wavelengths of BODIPYs **1a-c**. It is also clear that excited-state electron transfer from the singlet excited state of ^{1}BODIPY* to TMDs (reductive electron-transfer path), resulting in the charge-separated state TMD$^{\bullet+}$-BODIPY$^{\bullet-}$, is thermodynamically feasible. Importantly, such excited-state charge-separation could also be accomplished by excited TMDs, formed as a result of energy transfer.

Spectral identification of the electron-transfer products during transient absorption studies is essential, especially for hybrids **2a-c** and **3a-c**. Spectroelectrochemical experiments at the first oxidative potentials clearly show broad absorption peaks corresponding to **1a**$^{\bullet+}$ at 498 nm, **1b**$^{\bullet+}$ at 630 nm, and **1c**$^{\bullet+}$ at 600 nm (Figure S11). In contrast, no distinct new peaks were observed under the first reductive potentials (Figure S12). Slight variation in optical density, with decreased absorption in the 300–400 nm range, for MoS_2 and WS_2 oxidation was observed in the exfoliated materials (Figure S13), resulting in no major new peaks.

Next, femtosecond transient absorption (fs-TA) spectral studies in argon atmosphere were performed to seek evidence of energy and electron-transfer events. In the event of energy- or electron-transfer, faster recovery of the stimulated emission peak of BODIPY derivatives in hybrids **2a-c** and **3a-c** is expected, compared to pristine BODIPY. In the event of electron transfer, signature peaks corresponding to the radical anion of BODIPY and the radical cation of TMDs are also expected, or the relaxation dynamics would change appreciably. Figure 7a shows the fs-TA spectra of **1a** at the indicated delay times in DMF at the excitation wavelength of 480 nm, corresponding to the main absorption peak of **1a**. A negative peak in the 500 nm range, attributed to contributions from both ground state bleaching (GSB) and stimulated emission (SE), was observed. No strong peaks corresponding to excited state absorption (ESA) within the monitoring window were observed. The recovery of this peak was slow, which agreed well with the relatively long lifetime of **1a**, being 3.33 ns obtained by the time-correlated single photon counting technique (monoexponential decay). In agreement with earlier reports [15], immediately after 480 nm irradiation, the fs-TA spectra of MoS_2 show two main minima at 637 and 696 nm due to excitonic transitions as seen in the absorption spectrum, and two maxima at 595 and 663 nm corresponding to induced absorption of B and A excitons (Figure 7b). During the first 10 ps, all peaks experienced a blueshift, ascribed to cooling of hot excitons and/or interexcitonic interactions. Similarly, exfoliated WS_2 shows two minima at 545 and 652 nm (B and A excitons) and two maxima at 516 and 617 nm (Figure S14a), experiencing a blueshift of 2–3 nm, within the first 10 ps. In both cases of TMDs, the positive and negative peaks relaxed slowly. Next, **1b** revealed ESA peaks at 588 and 738 nm, along with a GSB/SE peak at 676 nm (Figure S15a). The decay and recovery of the ESA and GSB/SE peaks showed a new peak at 548 nm, corresponding to ^{3}**1b*** formed via intersystem crossing (ISC). The instantaneously formed ^{1}**1c*** exhibited ESA peaks at 557 and 654 nm, along with a broad negative feature centered at 704 nm, which, at longer delay times, split into distinct signals at 690 and 755 nm, corresponding GSB and SE, respectively (Figure S16a). The ESA peak also experienced a slight blueshift at 551 nm,

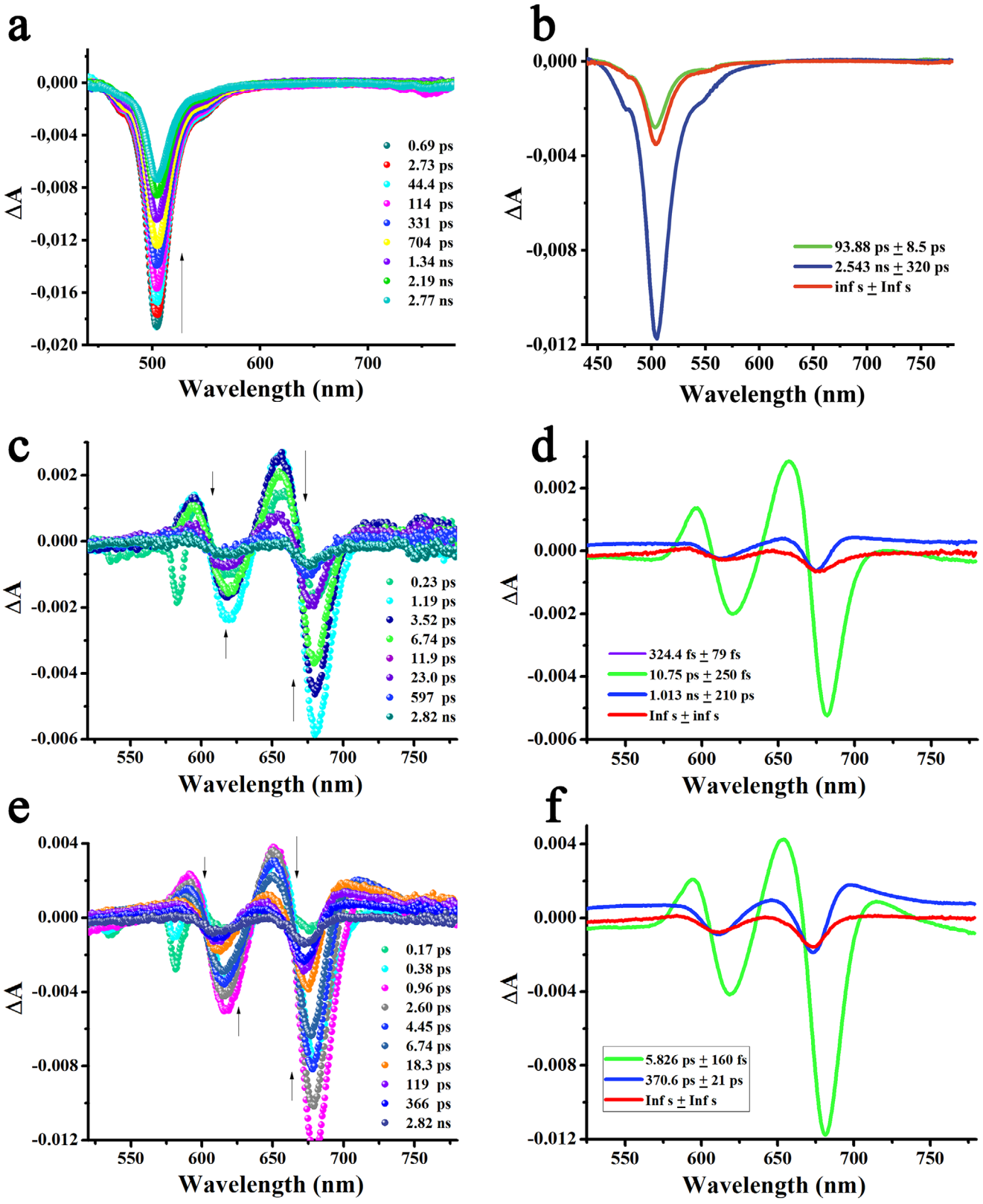

FIGURE 7 | Fs-TA spectra at the indicated delay times of (a) BODIPY **1a**, (b) exfoliated MoS_2, and (c) hybrid **2a** in DMF, and at the excitation wavelength of 480 nm. (d–f) The corresponding decay-associated spectra.

likely due to the contribution from ^{3}**1c*** formed via the ISC process.

Fs-TA spectra of **2a** and **3a** in DMF, excited at 480 nm, are shown in Figure 7c and Figure S14b, respectively, whereas of **2b-c** ad **3b-c** in Figures S15c,e and S16c,e, respectively. In **2a** and **3a,** the GSB/SE peak of **1a**, expected in the 500 nm range, was completely absent, suggesting faster timescale relaxation times than the earliest delay time that our instrument can measure (~ 1 ps). Since excited energy-transfer was expected, based on spectral overlap between BODIPY **1a** and both MoS_2 and WS_2, it is conceivable that ultrafast energy-transfer occurs ($k_{EnT} > 10^{12}$ s^{-1}) in hybrids **2a** and **3a**, populating the excited-state of MoS_2 and WS_2, respectively (Figure 6). This seems to be the case, wherein transient bands expected for MoS_2 and WS_2 appeared in less than 1 ps, indicating the occurrence of efficient excitation transfer. The decay/recovery of the transient bands of MoS_2 and WS_2 was similar to that of the exfoliated TMDs, namely, those without attached BODIPY. This is conceivable since the loading of BODIPY **1a** onto hybrids **2a** and **3a** is low, hence, TMDs carried **1a** only at the periphery of the nanosheets. No new bands were observed as those expected for BODIPY$^{\bullet-}$ and TMD$^{\bullet+}$ were too weak or nonexistent in the monitoring optical window. Only the timescale of the relaxation dynamics would indirectly shed light on such an occurrence. Similar conclusions can be drawn for hybrids **2b-c** and **3b-c**.

Further, the transient data were subjected to global target analysis (GloTarAn), and time constants for different events were evaluated. Three-component fit representing $S_0 \rightarrow S_1 \rightarrow T_1$ was satisfactory for **1a-c**, with lifetimes of 2.54 ns, 16.6 ps, and 1.58 ns, respectively, which agreed well with the fluorescence lifetime obtained from TCSPC (Figure 7d; Figures S15b and S16b) [38]. Interestingly, a three-component fit provided a satisfactory model for MoS_2 and WS_2 (Figure 7e; Figure S14c), yielding excited-state lifetimes of 1.01 and 1.08 ns, respectively. However, in the corresponding hybrids **2a** and **2b**, the lifetimes were significantly shortened to 370.6 and 410.3 ps, respectively, in the same order (Figure 7f; Figure S15d), indicating participation in electron transfer processes involving the appended BODIPYs **1a** and **1b**. Similar trends were observed in hybrid **2c** (Figure S16c,d), and **3a-c** (Figures S14b,d,S15e,f and S16e,f), which exhibited lifetimes of 458.3 and 593.0 ps, 423.5 and 682.2 ps, respectively. These observations support the occurrence of electron transfer from MoS_2 or WS_2 to BODIPYs.

To summarize the transient absorption spectral data, in all TMD-BODIPY hybrids **2a-c** and **3a-c**, ultrafast energy-transfer from ^{1}BODIPY* to TMDs is witnessed. Subsequent electron-transfer from excited TMD to BODIPY, leading to the formation of thermodynamically feasible charge-separated state TMD$^{\bullet+}$-BODIPY$^{\bullet-}$ was envisioned. This process resulted in faster relaxation of TMDs excitonic state, within hybrids **2a-c** and **3a-c**. Notably, MoS_2-BODIPY hybrids **2a-c** exhibited greater lifetime shortening, consistent with the fact that WS_2 is more difficult to oxidize. Furthermore, the presence of electron-donating groups such as PTZ and TPA in BODIPY derivatives **1b** and **1c** appears to mitigate lifetime shortening compared to methyl-substituted BODIPY **1a**. Certainly, the introduction of electron-donating groups such as PTZ and TPA increases the charge density on the BODIPY core, reducing the overall electron-accepting character of the dye, which may partially hinder the electron-transfer process. Hence, the electronic interactions between BODIPY derivatives and TMDs remained invariant, regardless of the spectroscopic region targeted, the nature of the TMDs, or their electron-donating/accepting character. This suggests that the aromatic skeleton of BODIPYs is the primary driver of the electron-transfer process. This is further evidenced by electrochemistry via the redox data and bandgap values collected (Table S1) [15, 37, 38]. In fact, the current energy transfer followed by an electron transfer mechanism observed in TMD-BODIPY can be described using a traditional band alignment [41] but only when the trap states present in MoS_2 and WS_2 are taken into account [16, 42]. These trap states, whether electronically empty or occupied depending on their position relative to the Fermi level, enable the formation of a type I–like alignment. This allows the generation of photocarriers not directly from the valence band maximum (VBM) to the conduction band minimum (CBM) of TMDs, but via the trap states [16, 42]. Additionally, electron transfer from the CBM of TMDs to the LUMO of **1a-c**, enabling the formation of radical ion pair TMD$^{\bullet+}$-BODIPY$^{\bullet-}$ occurs. A representative diagram, with an expanded description, is shown in Figure S17. Based on the time constant of MoS_2 and WS_2 in the corresponding hybrids **2a-c** and **3a-c**, respectively, electron-transfer rates ($k_{ET} = 1/\tau_{hybrid} - 1/\tau_{ref}$, where τ_{ref} is the lifetime of exfoliated TMDs) were estimated and found to range 1–2 × 10^9 s^{-1}. The relatively efficient k_{ET} suggests their use in light energy harvesting applications [7]. It is worth mentioning here that due to the heterogeneity of the investigated samples, no attempts were made to correlate the electron transfer dynamics to the structure of TMD-BDP systems.

The energy and electron transfer events by BODIPYs in TMDs may be of great interest in several areas of nanotechnology [10]. Indeed, MoS_2 or WS_2 covalently functionalized with quantum dots [17, 18] or Ni–porphyrin [21], respectively, have been shown to boost photocatalytic activity, owing to similar photoinduced carrier processes. Moreover, other chromophores such as pyrene [39], perylene [19], PCBM [16], or ZnP [20] have been proven to substantially enhance photoresponse, while also improving stability. Considering that long-term stability is critical for real-world energy harvesting applications and acknowledging that it remains one of the weakest points in TMDs produced by methods such as CVD [16, 19, 20], our last experiments focused on analyzing the quality of the so-formed hybrids after being exposed to air and moisture for more than four years. In short, the Raman spectra of aged **2a-c** and **3a-c** are identical to those of fresh materials, showing negligible amounts of MoO_x (800–1000 cm^{-1}) and WO_x (600–850 cm^{-1}), respectively (Figure S18), exhibiting no detectable signs of degradation [43, 44].

3 | Conclusion

In this contribution, we employ classic organic chemistry to derivatize BODIPY with methyl, PTZ, and TPA units, as well as to introduce the 1,2-dithiolane linker, capable of being covalently grafted onto chemically exfoliated MoS_2 and WS_2, en route to the realization of advanced hybrid materials **2a-c** and **3a-c**, respectively, with intriguing electronic properties. As envisioned from the energy level diagram, ultrafast energy transfer from ^{1}BODIPY* to TMD was witnessed from the femtosecond pump-

probe technique. Subsequent radical signals corresponding to the charge-separated state were within the strong excitonic signals of TMD; however, faster relaxation of the TMD signals was supportive of charge-separation primarily from the excited TMD. We firmly believe that the current strategy will contribute to a deeper understanding of the fundamentals of electron-transfer mechanisms in TMDs and aid in predicting the optical and electronic properties of hybrid materials, which are of interest for the development of light- and charge-transfer-related applications [7, 10].

Acknowledgements

The research project was supported by the Hellenic Foundation for Research and Innovation (H.F.R.I.) under the "Second Call for H.F.R.I. Research Projects to support Faculty Members & Researchers" (Project Number 2482). FD is thankful to the US National Science Foundation for financial support (Grant Nos. 2345836 and 2514911).

The publication of this article in OA mode was financially supported by HEAL-Link.

Conflicts of Interest

The authors declare no conflicts of interest.

Data Availability Statement

The data that support the findings of this study are available in the supporting information and also from the corresponding author upon reasonable request.

References

1. A. Chaves, J. G. Azadani, H. Alsalman, et al., "Bandgap Engineering of Two-Dimensional Semiconductor Materials," *npj 2D Materials and Applications* 4 (2020): 29.

2. S. Golovynskyi, O. I. Datsenko, D. Dong, et al., "Trion Binding Energy Variation on Photoluminescence Excitation Energy and Power During Direct to Indirect Bandgap Crossover in Monolayer and Few-Layer MoS_2," *The Journal of Physical Chemistry C* 125 (2021): 17806–17819, https://doi.org/10.1021/acs.jpcc.1c04334.

3. H. Zhang, M. Chhowalla, and Z. Liu, "2D Nanomaterials: Graphene and Transition Metal Dichalcogenides," *Chemical Society Reviews* 47 (2018): 3015–3017, https://doi.org/10.1039/C8CS90048E.

4. S. Tanwar, A. Arya, A. Gaur, and A. L. Sharma, "Transition Metal Dichalcogenide (TMDs) Electrodes for Supercapacitors: A Comprehensive Review," *Journal of Physics-Condensed Matter* 33 (2021): 303002.

5. H. S. Nalwa, "A Review of Molybdenum Disulfide (MoS_2) Based Photodetectors: From Ultra-Broadband, Self-Powered to Flexible Devices," *RSC Advances* 10 (2020) 30529–30602.

6. A. Stergiou and N. Tagmatarchis, "Molecular Functionalization of Two-Dimensional MoS_2 Nanosheets," *Chemistry—A European Journal* 24 (2018): 18246–18257, https://doi.org/10.1002/chem.201803066.

7. C. Stangel, E. Nikoli, and N. Tagmatarchis, "Transition Metal Dichalcogenides Interfacing Photoactive Molecular Components for Managing Energy Conversion Processes," *Advanced Energy and Sustainability Research* 3 (2022): 2200097, https://doi.org/10.1002/aesr.202200097.

8. S. Ippolito and P. Samorì, "Defect Engineering Strategies Toward Controlled Functionalization of Solution-Processed Transition Metal Dichalcogenides," *Small Science* 2 (2022): 2100122, https://doi.org/10.1002/smsc.202100122.

9. R. Canton-Vitoria, Y. Sayed-Ahmad-Baraza, M. Pelaez-Fernandez, et al., "Functionalization of MoS_2 With 1,2-dithiolanes: Toward Donor-Acceptor Nanohybrids for Energy Conversion," *Npj 2D Materials and Applications* 1 (2017): 13, https://doi.org/10.1038/s41699-017-0012-8.

10. H. Imahori and M. Akiyama, "Photoinduced Charge Separation at Heterojunctions Between Two-Dimensional Layered Materials and Small Organic Molecules," *Materials Horizons* 2025, 12, 92–102.

11. R. Canton-Vitoria, T. Scharl, A. Stergiou, et al., "Ping-Pong Energy Transfer in Covalently Linked Porphyrin-MoS_2 Architectures," *Angewandte Chemie International Edition* 59 (2020): 3976–3981, https://doi.org/10.1002/anie.201914494.

12. R. Canton-Vitoria, H. B. Gobeze, V. M. Blas-Ferrando, et al., "Excited-State Charge Transfer in Covalently Functionalized MoS_2 With a Zinc Phthalocyanine Donor–Acceptor Hybrid," *Angewandte Chemie International Edition* 58 (2019): 5712–5717, https://doi.org/10.1002/anie.201900101.

13. T. Umeyama, D. Mizutani, Y. Ikeda, et al., "An Emissive Charge-Transfer Excited-State at the Well-Defined Hetero-Nanostructure Interface of an Organic Conjugated Molecule and Two-Dimensional Inorganic Nanosheet," *Chemical Science* 14 (2023): 11914–11923, https://doi.org/10.1039/D3SC03604A.

14. I. K. Sideri, Y. Jang, J. Garcés-Garcés, et al., "Unveiling the Photoinduced Electron-Donating Character of MoS_2 in Covalently Linked Hybrids Featuring Perylenediimide," *Angewandte Chemie International Edition* 60 (2021): 9120–9126, https://doi.org/10.1002/anie.202016249.

15. L. Vallan, R. Canton-Vitoria, H. B. Gobeze, et al., "Interfacing Transition Metal Dichalcogenides With Carbon Nanodots for Managing Photoinduced Energy and Charge-Transfer Processes," *Journal of the American Chemical Society* 140 (2018): 13488–13496, https://doi.org/10.1021/jacs.8b09204.

16. R. Canton-Vitoria and R. Kitaura, "Insulating 6, 6-Phenyl-C61-butyric Acid Methyl Ester on Transition-Metal Dichalcogenides: Impact of the Hybrid Materials on the Optical and Electrical Properties," *Chemistry—A European Journal* 30 (2024): 202400150.

17. A. Kagkoura, R. Canton-Vitoria, L. Vallan, et al., "Bottom-Up Synthesized MoS_2 Interfacing Polymer Carbon Nanodots With Electrocatalytic Activity for Hydrogen Evolution," *Chemistry—A European Journal* 26 (2020): 6635–6642, https://doi.org/10.1002/chem.202000125.

18. R. Canton-Vitoria, L. Vallan, E. Urriolabeitia, A. M. Benito, W. K. Maser, and N. Tagmatarchis, "Electronic Interactions in Illuminated Carbon Dot/MoS 2 Ensembles and Electrocatalytic Activity Towards Hydrogen Evolution," *Chemistry—A European Journal* 24 (2018): 10468–10474, https://doi.org/10.1002/chem.201801425.

19. R. Canton-Vitoria, Y. Matsunaga, S. Zhang, M. Xue, M. Osada, and R. Kitaura, "Covalent Functionalization of Transition Metal Dichalcogenides With Perylene for Light Harvesting Devices," *Nanoscale* 17 (2025): 8084–8100, https://doi.org/10.1039/D4NR05364H.

20. R. Canton-Vitoria, T. Hotta, Y. Tanuma, et al., "Localized Excitons in Zn-Porphyrin Covalently Functionalized MoS_2 and WS_2," *The Journal of Physical Chemistry C* 127 (2023): 10699–10708, https://doi.org/10.1021/acs.jpcc.2c08009.

21. M. P. Minadakis, R. Canton-Vitoria, C. Stangel, et al., "Tungsten Disulfide-Interfacing Nickel-Porphyrin for Photo-Enhanced Electrocatalytic Water Oxidation," *Chemsuschem* 16 (2023): 202202322.

22. R. Canton-Vitoria, K. Sato, Y. Motooka, S. Toyokuni, Z. Liu, and R. Kitaura, "Field-Effect Transistor Antigen/Antibody-TMDs Sensors for the Detection of COVID-19 Samples," *Nanoscale* 15 (2023): 4570–4580, https://doi.org/10.1039/D2NR06630K.

23. R. Canton-Vitoria, C. Stangel, and N. Tagmatarchis, "Electrostatic Association of Ammonium-Functionalized Layered-Transition-Metal Dichalcogenides With an Anionic Porphyrin," *ACS Applied Materials & Interfaces* 10 (2018): 23476–23480, https://doi.org/10.1021/acsami.8b08272.

24. R. Canton-Vitoria, E. Istif, J. Hernández-Ferrer, et al., "Integrating Water-Soluble Polythiophene With Transition-Metal Dichalcogenides for Managing Photoinduced Processes," *ACS Applied Materials & Interfaces* 11 (2019): 5947–5956, https://doi.org/10.1021/acsami.8b18435.

25. N. Boens, V. Leen, and W. Dehaen, "Fluorescent indicators based on BODIPY," *Chemical Society Reviews* 41 (2012): 1130–1172, https://doi.org/10.1039/C1CS15132K.

26. M. Tsigkou, E. Nikoli, I. K. Sideri, et al., "Electronic Interactions in Coulombic Associated Photoactive Macrocycles to Chemically Modified MoS_2 Nanosheets," *Chemistry—A European Journal* 31 (2025): 202404746, https://doi.org/10.1002/chem.202404746.

27. A. Arcidiacono, C. R. Johnston, C. L. Keenan, et al., "Functionalization of Monolayer MoS_2 With Layered Multimolecular Architectures," *ACS Applied Optical Materials* 2 (2024): 2011–2018, https://doi.org/10.1021/acsaom.4c00327.

28. P. Behera, S. Karunakaran, J. Sahoo, P. Bhatt, S. Rana, and M. De, "Ligand Exchange on MoS_2 Nanosheets: Applications in Array-Based Sensing and Drug Delivery," *ACS Nano* 17 (2023): 1000–1011, https://doi.org/10.1021/acsnano.2c06994.

29. Y. Tutel, G. Sevinç, B. Küçüköz, et al., "Ultrafast Electron/Energy Transfer and Intersystem Crossing Mechanisms in BODIPY-Porphyrin Compounds," *Processes* 9 (2021): 312, https://doi.org/10.3390/pr9020312.

30. J.-Y. Liu, Y. Huang, R. Menting, B. Röder, E. A. Ermilov, and D. K. Ng, "A boron Dipyrromethene–Phthalocyanine Pentad as an Artificial Photosynthetic Model," *Chemical Communications* 49 (2013): 2998, https://doi.org/10.1039/c3cc00262d.

31. C. A. Wijesinghe, M. E. El-Khouly, J. D. Blakemore, M. E. Zandler, S. Fukuzumi, and F. D'Souza, "Charge Stabilization in a Closely Spaced Ferrocene–Boron Dipyrrin–Fullerene Triad," *Chemical Communications* 46 (2010): 3301, https://doi.org/10.1039/c000565g.

32. F. D'Souza, P. M. Smith, M. E. Zandler, et al., "Energy Transfer Followed by Electron Transfer in a Supramolecular Triad Composed of Boron Dipyrrin, Zinc Porphyrin, and Fullerene: A Model for the Photosynthetic Antenna-Reaction Center Complex," *Journal of the American Chemical Society* 126 (2004): 7898–7907.

33. F. D'Souza, C. A. Wijesinghe, M. E. El-Khouly, et al., "Ultrafast Excitation Transfer and Charge Stabilization in a Newly Assembled Photosynthetic Antenna-Reaction Center Mimic Composed of Boron Dipyrrin, Zinc Porphyrin and Fullerene," *Physical Chemistry Chemical Physics* 13 (2011): 18168–18178.

34. D. Badgurjar, S. Seetharaman, F. D'Souza, and R. Chitta, "One-Photon Excitation Followed by a Three-Step Sequential Energy–Energy–Electron Transfer Leading to a Charge-Separated State in a Supramolecular Tetrad Featuring Benzothiazole–Boron-Dipyrromethene–Zinc Porphyrin–C 60," *Chemistry—A European Journal* 27 (2020): 2184–2195, https://doi.org/10.1002/chem.202004262.

35. R. Canton-Vitoria, A. Z. Alsaleh, G. Rotas, et al., "Graphene Performs the Role of an Electron Donor in Covalently Interfaced Porphyrin-Boron Azadipyrromethene Dyads and Manages Photoinduced Charge-Transfer Processes," *Nanoscale* 14 (2022): 15060–15072, https://doi.org/10.1039/D2NR03740H.

36. G. Rotas, M. B. Thomas, R. Canton-Vitoria, F. D'Souza, and N. Tagmatarchis, "Preparation, Photophysical and Electrochemical Evaluation of an Azaborondipyrromethene/Zinc Porphyrin/Graphene Supramolecular Nanoensemble," *Chemistry—A European Journal* 26 (2020): 6652–6661, https://doi.org/10.1002/chem.202000174.

37. S. Shao, H. B. Gobeze, P. A. Karr, and F. D'Souza, "Ultrafast Photoinduced Charge Separation in Wide-Band-Capturing Self-Assembled Supramolecular Bis(donor styryl)BODIPY–Fullerene Conjugates," *Chemistry—A European Journal* 21 (2015): 16005–16016, https://doi.org/10.1002/chem.201502395.

38. C. O. Obondi, G. N. Lim, P. A. Karr, V. N. Nesterov, and F. D'Souza, "Photoinduced Charge Separation in Wide-Band Capturing, Multi-Modular Bis(Donor Styryl)BODIPY–Fullerene Systems," *Physical Chemistry Chemical Physics* 18 (2016): 18187–18200, https://doi.org/10.1039/C6CP03479A.

39. R. Canton-Vitoria, S. Nufer, X. Che, et al., "Pyrene-Functionalized Tungsten Disulfide as Stable Resistive Photosensor," *Materials Advances* 1 (2020): 2459–2466, https://doi.org/10.1039/D0MA00429D.

40. Y. Huang, F. Zhuge, J. Hou, et al., "Van der Waals Coupled Organic Molecules With Monolayer MoS_2 for Fast Response Photodetectors With Gate-Tunable Responsivity," *ACS Nano* 12 (2018): 4062–4073, https://doi.org/10.1021/acsnano.8b02380.

41. S. Dutta, R. Canton-Vitoria, S. Shao, N. Tagmatarchis, and F. D'Souza, "Hybrid Nanostructures by Covalent Functionalization of MoS_2 and WS_2 with C60 Undergoing Excited Electron Transfer," *Chemistry–A European Journal* 31 (2025): 02758, https://doi.org/10.1002/chem.202502758.

42. I. K. Sideri, R. Canton-Vitoria, H. J. Ojeda-Galvan, M. Quintana, and N. Tagmatarchis, "Sustainable Photocatalytic Acylation of Transition Metal Dichalcogenides With Atom Economy," *Small* 20 (2024): 2311045.

43. R. Canton-Vitoria, Y. Sayed-Ahmad-Baraza, R. Arenal, C. P. Ewels, and N. Tagmatarchis, "Pyrene Coating Transition Metal Disulfides as Protection From Photooxidation and Environmental Aging," *Nanomaterials* 10 (2020): 363, https://doi.org/10.3390/nano10020363.

44. R. Canton-Vitoria, T. Hotta, M. Xue, S. Zhang, and R. Kitaura, "Synthesis and Characterization of Transition Metal Dichalcogenide Nanoribbons Based on a Controllable O_2 Etching," *Journal of the American Chemical Society Au* 3 (2023): 775–784.

Supporting Information

Additional supporting information can be found online in the Supporting Information section.

Supporting File: smll71960-sup-0001-SuppMat.pdf